



Traveling and standing thermoacoustic waves in solid media

Haitian Hao^{a,b}, Carlo Scalo^a, Fabio Semperlotti^{a,b,*}

^a School of Mechanical Engineering, Purdue University, West Lafayette, IN 47907, USA

^b Ray W. Herrick Laboratories, 177 South Russell Street, West Lafayette, IN 47907, USA

ARTICLE INFO

Article history:

Received 14 June 2018

Revised 18 October 2018

Accepted 20 February 2019

Available online 24 February 2019

Handling Editor: J. Astley

Keywords:

Solid state

Thermoacoustics

Traveling wave

Energy conversion

ABSTRACT

The most attractive application of fluid-based thermoacoustic (TA) energy conversion involves traveling wave devices due to their low onset temperature ratios and high growth rates. Recently, theoretical and numerical studies have shown that thermoacoustic effects can exist also in solids. However, these initial studies only focus on standing waves. This paper presents a numerical study investigating the existence of self-sustained thermoelastic oscillations associated with traveling wave modes in a looped solid rod under the effect of a localized thermal gradient. Configurations having different ratios of the rod radius R to the thermal penetration depth δ_k were explored and the traveling wave component (TWC) was found to become dominant as R approaches δ_k . The growth-rate-to-frequency ratio of the traveling TA wave is found to be significantly larger than that of the standing wave counterpart for the same wavelength. The perturbation energy budgets are analytically formulated and closed, shedding light onto the energy conversion processes of solid-state thermoacoustic (SSTA) engines and highlighting differences with fluids. Efficiency is also quantified based on the thermoacoustic production and dissipation rates evaluated from the energy budgets.

© 2019 Elsevier Ltd. All rights reserved.

1. Introduction

Thermoacoustic (TA) instability is a thermodynamic process through which heat is converted into mechanical energy [1]. When the working medium is a fluid, this process can be driven by combustion [2] or, more simply, by wall heat transfer [3]. In both cases, a two-way coupling between fluid motion and fluctuations in heat release rates is established, effectively resulting in a thermodynamic cycle where the fluid parcel produces mechanical (acoustic) work. This inherently cyclic process makes pressure and velocity oscillations grow unbounded in the absence of losses. Recently, Hao et al. [4] have theoretically demonstrated that this process can also occur with elastic waves in solid media. They provided theoretical and numerical evidence of the existence of thermoacoustic instability in solids by showing unbounded standing wave oscillations in a quarter-wavelength (fixed-free) and a sub-quarter-wavelength (fixed-mass) metal rod.

The present manuscript provides two key contributions: 1) it extends the concept of solid-state thermoacoustics (SS-TA) to traveling wave configurations, and 2) offers an in-depth analysis of the wave energy budgets of SS-TA. Thermoacoustic instability, in fact, can be exploited to design energy conversion devices called thermoacoustic engines (TAEs) [5], which are categorized into two types: standing-wave and traveling-wave engines. The difference between them lies in the phase difference between pressure and velocity oscillations. In a standing wave device, the phase difference is approximately (but not exactly equal to) 90° at all spatial locations, while in a traveling wave engine it stays well below 90° depending on the specific design (e.g. between $\pm 30^\circ$ in the traveling wave TAE built by Yazaki [6]). The efficiency is greatly affected by the relative phasing of the oscillations.

* Corresponding author. School of Mechanical Engineering, Purdue University, West Lafayette, IN 47907, USA.

E-mail addresses: haoh@purdue.edu (H. Hao), scalo@purdue.edu (C. Scalo), fsemperl@purdue.edu (F. Semperlotti).

Ceperley [7] was the first to propose that a very efficient pistonless Stirling-like thermodynamic cycle could be achieved with traveling waves propagating through a solid boundary with thermal gradient. Such an engine was experimentally designed by Yazaki et al. [6] although at a relatively low efficiency compared to Ceperley's theoretical expectations [7]. Backhaus and Swift [8] later designed a new type of traveling-wave TAE based on a compact acoustic network. The addition of a resonator superimposes standing waves on the traveling wave in the engine to decrease the large loss observed in both Ceperley's and Yazaki's designs.

While exhibiting higher thermoacoustic growth rates, traveling-wave TAEs suffer from nonlinear losses such as Gedeon Streaming and other forms of acoustic streaming [9–14], found to be the main cause of efficiency drop.

In this study, we prove the existence of traveling thermoacoustic waves in solid media based on the theoretical framework developed previously by the same authors [4]. We also show that the growth-rate-to-frequency ratio (shorten as growth ratio hereinafter) of the traveling wave oscillations is considerably larger than that of a standing wave oscillation of the same wavelength. Heat flux, mechanical power, and work source for theoretical solid-state thermoacoustic (SSTA) engines are defined heuristically in light of their definitions in fluids. The acoustic energy budgets are analyzed in detail to interpret the energy conversion process in SSTA engines and to define the efficiencies of SSTA engines. Through the detailed study and comparison of traveling and standing wave thermoacoustics, this paper expands the theory of thermoacoustics of solids and may lead to implementations of new generations of ultra-compact and robust SSTA devices capable of direct thermal-to-mechanical energy conversion.

2. Problem statement

In this study, we consider two configurations (Fig. 1) in which a ring-shaped slender metal rod with circular cross section is under investigation. Specifically, they are called the looped rod (Fig. 1(a) and (c)) and the resonance rod (Fig. 1(b) and (d)). The rod experiences an externally imposed axial thermal gradient applied via isothermal conditions on its outer surface at a certain location, while the remaining exposed surfaces are adiabatic. The difference between the two configurations lies in the imposition of a displacement/velocity node (Fig. 1(d)), which is used in the resonance rod to suppress the traveling wave mode. Practically, the displacement node could be realized by constraining the rod with a clamp at a proper location (Fig. 1(b)). The

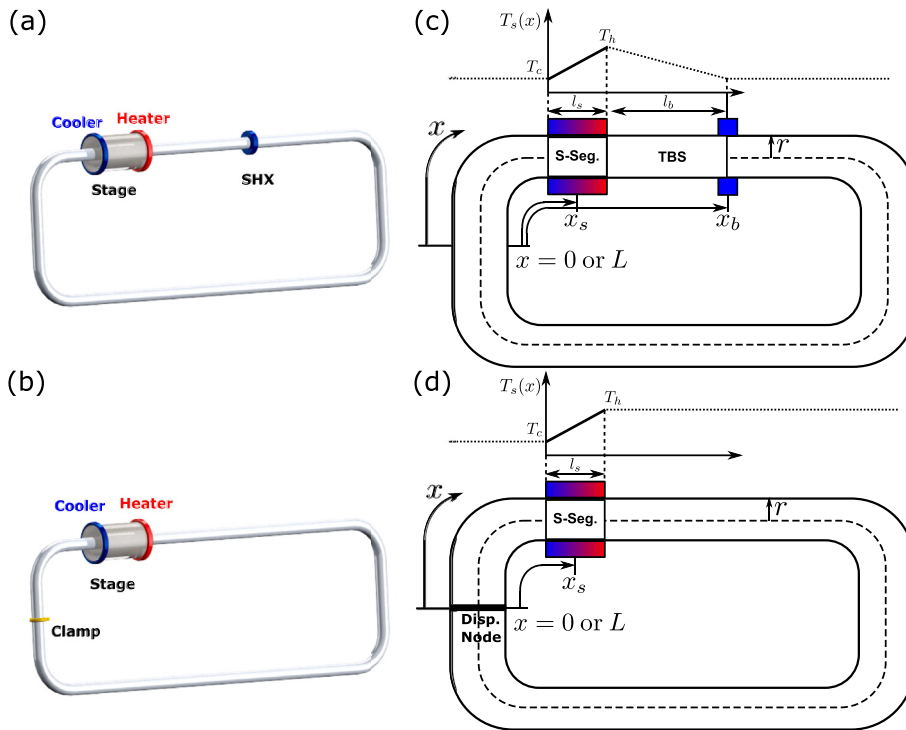


Fig. 1. Notional schematics of (a) the looped rod and (b) the resonance rod. A component with a large thermal inertia, stage, connected to a heater and a cooler on opposite ends, is mounted on the outer surface of the rod to sustain a linear thermal gradient. In (a), a secondary cold heat exchanger (SHX) is attached to the rod creating the Thermal Buffer Segment (TBS, shown in (c)). In (b), a clamp is used to apply the displacement node (abbreviated as Disp. Node in (d)), which is necessary to suppress the traveling wave mode. (c) and (d) show the temperature profile $T_s(x)$ in the S-seg. (solid line, $T_s(x)$), and in the remaining sections (dashed line), and the characteristic geometric parameters. T_h and T_c are the hot and cold temperatures respectively. The stage is $l_s = 0.05L$ long centered about $x = x_s$ (irrelevant for the looped design). The SHX is mounted at x_b ($l_b = 0.45L$ away from the stage). The optimal location of the stage's midpoint x_s for the full-wavelength standing wave is $x_s = 0.845L$.

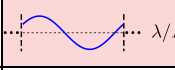
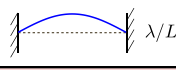
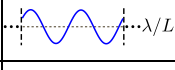
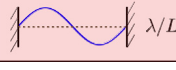
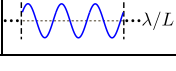
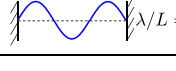
Mode No.	Looped rod (Loop)	Resonance rod (Res)
I		
II		
III		

Fig. 2. The mode shapes of the looped and the resonance rod and the naming convention for modes. Note that same mode numbers correspond to different wavelengths. Especially, the looped rod starts with a full-wavelength mode as its first mode while a resonance rod starts with a half-wavelength one. To make a comparison based on the same wavelength, *Loop – I* and *Res – II* represent our contrast group (the shaded blocks).

coupled thermoacoustic response induced by the external thermal gradient and the initial mechanical excitation is investigated.

The initial mechanical excitation could grow with time as a result of the coupling between the mechanical and thermal response provided a sufficient temperature gradient is imposed on the outer boundary of a solid rod at a proper location. This phenomenon is identified as the thermoacoustic response of solids in Ref. [4].

By analogy with fluid-based traveling wave thermoacoustic engines [6,15], a stage element is used to impose a thermal gradient on the surface of the looped rod (Fig. 1(a)). The specific location of the stage element in this case is irrelevant due to the periodicity of the system. The segment surrounded by the stage is named S-segment, which experiences a spatial temperature gradient (from T_c to T_h) due to the externally enforced temperature distribution. The interface between the stage and the S-segment is ideally assumed to have a high thermal conductivity, which assures the isothermal boundary conditions along with a zero shear stiffness. One can anticipate the compromise between these two seemingly contradictory conditions in an experimental validation. The stage is considered as a thermal reservoir so that the temperature fluctuation on the surface of S-segment is assumed to be zero (isothermal). A Thermal Buffer Segment (TBS) next to the thermal gradient provides a thermal buffer between T_h and room temperature T_c . The temperature drop in the TBS is caused by the secondary cold heat exchanger (SHX, Fig. 1(a)) located at x_b . A linear temperature profile in the TBS from T_h to T_c is adopted to account for the natural axial thermal conduction along the looped rod.

To show the superiority of traveling wave thermoacoustics, a fair comparison was conducted with a resonance rod. The resonance rod, as Fig. 1(d) shows, was constructed by enforcing a displacement/velocity node at an arbitrary position labeled $x = 0$. This node is equivalent to a fixed and adiabatic boundary condition. If only plane wave propagation is considered, this resonance rod has no difference with a straight rod with both ends clamped. The TBS is not necessary in the resonance rod since the temperature can be discontinuous at the displacement node. To make a comparison, we calculated the growth ratio of a standing wave mode in the resonance rod with the same wavelength ($\lambda = L$) and frequency (≈ 2830 Hz) as the traveling wave mode in the looped rod without the displacement node. We highlight the essential difference of the mode numbering in Fig. 2 and propose a naming convention for the modes for brevity. The modes in comparison in this study are *Loop – I* and *Res – II* (the shaded blocks).

With the boundary conditions well defined, the governing equations can be solved to show the transient thermoacoustical response of the system.

3. Mathematical modeling

The laws of thermoelasticity are considered to model thermoacoustics in solids in that an elastic wave propagating in a solid medium, whether growing or decaying, is accompanied by a thermal wave. The essential difference with previous studies in thermoelasticity is the presence of heat exchange between the solid medium and its boundary. Hao et al. [4] discovered that thermoelastic waves can be made thermoacoustically unstable. In the following, we analyze the thermoacoustic response of the setup in Fig. 1 adopting the previously developed thermoacoustic linear stability model [4] according to Rott's theory [16].

In a one dimensional solid rod, the conservation of momentum is written as

$$\frac{\partial v}{\partial t} = \frac{1}{\rho} \frac{\partial \sigma}{\partial x}, \quad (1)$$

where v and σ are the particle velocity and stress, respectively, ρ is the material density. The stress σ can be expressed as

$$\sigma = E \left[\frac{\partial u}{\partial x} - \alpha(T - T_0) \right], \quad (2)$$

where E is Young's modulus, u is the particle displacement, α is the thermal expansion coefficient, T and T_0 are the temperature of the material and the reference temperature. The stress σ is intended as positive if a solid element is locally in traction. This is in contrast with pressure fluctuations in fluids, which are intended as positive when compressive.

In the system shown in Fig. 1, the heat exchange mainly occurs in the radial direction in the S-segment, so the energy conservation can be written as

$$\frac{\partial T}{\partial t} + \frac{\partial T}{\partial x} v = -\gamma_G T \frac{\partial v}{\partial x} + \frac{\kappa}{\rho c_e} \frac{1}{r} \frac{\partial}{\partial r} \left(r \frac{\partial T}{\partial r} \right), \quad (3)$$

where c_e is the specific heat at constant strain, κ is the thermal conductivity of the medium, $\gamma_G = \frac{\alpha E}{\rho c_e}$ is the one-dimensional Grüneisen constant [17]. The left hand side denotes the total derivative of T and the terms on the right hand side are the thermoelastic coupling term and the radial thermal conduction. The axial thermal conduction is neglected according to Rott's theory [16]. The linearized analysis is performed around mean state $\{u_0, v_0, T_0\} = \{0, 0, T_0\}$, where u, v and T are the particle displacement, particle velocity and temperature, the subscript 0 denotes *base state* because they are zero order terms. The solid is assumed to be homogeneous and isotropic. The first order fluctuating terms (with subscript '1') are assumed to be harmonic in time. By applying the cross-sectional averaging operator to all of the first order harmonic quantities in Eqs. (1) and (3) and transforming them into the frequency domain [4], namely $\langle ()_1 \rangle_r = \langle () - ()_0 \rangle_r = \hat{()e^{i\Lambda t}}$, where $\langle () \rangle_r$ indicates cross sectional averaging for quantities in the time domain, $\hat{()}$ refers to the cross-sectionally averaged fluctuating variables in the frequency domain, $\Lambda = -i\beta + \omega$, ω is the angular frequency of the harmonic response, and β is the growth rate, the linearized quasi-1D equations are written as

$$i\Lambda \hat{u} = \hat{v}, \quad (4)$$

$$i\Lambda \hat{v} = \frac{E}{\rho} \left(\frac{d^2 \hat{u}}{dx^2} - \alpha \frac{d\hat{T}}{dx} \right), \quad (5)$$

$$i\Lambda \hat{T} = -\frac{dT_0}{dx} \hat{v} - \gamma_G T_0 \frac{d\hat{v}}{dx} + i\omega g_k \hat{T}, \quad (6)$$

where i is the imaginary unit, \hat{u}, \hat{v} and \hat{T} are the fluctuations of the particle displacement, particle velocity, and temperature averaged over the cross section of the rod. The dimensionless function g_k is given by

$$g_k = \begin{cases} \frac{1}{1 - \frac{1}{2} \xi_{top} \frac{J_0(\xi_{top})}{J_1(\xi_{top})}} & x_s - \frac{l_s}{2} < x < x_s + \frac{l_s}{2} \\ 0 & \text{elsewhere} \end{cases}, \quad (7)$$

where $J_n(\cdot)$ are Bessel functions of the first kind, $\xi_{top} = \sqrt{-2i} \frac{R}{\delta_k}$ is the dimensionless complex radius, R is the radius of the looped rod. The thermal penetration depth δ_k is defined as $\delta_k = \sqrt{\frac{2\kappa}{\omega \rho c_e}}$. This quantity represents the characteristic thermal penetration depth from the isothermal boundary in the radial direction. The dimensionless function g_k incorporates the effects of the radial thermal conduction from the walls of the S-segment. The derivation of g_k can be found in Supplementary Material. The temperature fluctuation caused by the heat exchange between the solid media and SHX is neglected considering the small size of SHX. As a result, $g_k(x_b) = 0$.

An eigenvalue analysis $(i\Lambda \mathbf{I} - \mathbf{A})\mathbf{y} = \mathbf{0}$ was performed based on the linear quasi-1D model to find the angular frequency ω and growth rate β . In the eigenvalue problem, \mathbf{I} , \mathbf{A} and $\mathbf{0}$ are the identity matrix, coefficient matrix, and the null vector respectively, and $\mathbf{y} = [\hat{u}; \hat{v}; \hat{T}]$ is the vector of state variables where \hat{u}, \hat{v} , and \hat{T} are the eigenfunctions of \hat{u}, \hat{v} , and \hat{T} .

4. Results

We solved the eigenvalue problem numerically for both cases of a $L = 1.8$ m long aluminum rod, being the looped or the resonance rod, under a 200 K temperature difference ($T_h = 493.15$ K and $T_c = 293.15$ K) with a 0.05L long stage to investigate the thermoacoustic response of the system. The material properties of aluminum are chosen as: Young's modulus $E = 70$ GPa, density $\rho = 2700$ kg/m³, thermal expansion coefficient $\alpha = 23 \times 10^{-6}$ K⁻¹, thermal conductivity $\kappa = 238$ W/(m·K) and specific heat at constant strain $c_e = 900$ J/(kg·K).

The first traveling wave mode in the looped rod, with a full wavelength ($\lambda = L$) is considered, and will be referred to as *Loop - I*, following the naming convention of modes shown in Fig. 2. The dimensionless growth ratio β/ω is used as a metric of the SSTA engine's ability to convert heat into mechanical energy; such normalization accounts for the fact that thermoacoustic engines operating at high frequencies naturally exhibit high growth rates [18] and vice versa. Besides, in solids the inherent structural damping is commonly expressed as a fraction of the frequency of the oscillations, i.e. the damping ratio; the latter is widely used to quantify the frequency-dependent loss/dissipative effect in solids. The optimal growth ratio was found by gradually varying the radius R of the looped rod. We used the dimensionless radius R/δ_k to represent the effect of geometry, where δ_k was assumed to be constant at the operating frequency $f = \frac{c}{\lambda} \approx \frac{\sqrt{E/\rho}}{L} = 2830$ Hz. The '*Loop - I*' curve in Fig. 3 shows the growth ratio β/ω vs. the dimensionless radius R/δ_k of a full-wavelength traveling wave mode. The frequency variation with radius is neglected. Positive growth ratios are obtained in the absence of losses, and the losses in solids are mainly induced by intrinsic structural damping. The positive growth ratio suggests that the undamped system is capable of sustaining and

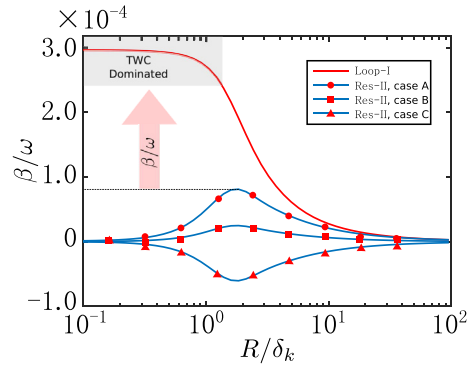


Fig. 3. A semilog plot of the growth ratio versus the nondimensional radius for the *Loop – I* mode in the looped rod and the *Res – II* mode in the resonance rod. Case A, B, C correspond to *Res – II* mode with the stage placed at different locations. The growth ratios of these three cases at optimal R/δ_k are plotted in Fig. 4.

amplifying the propagation of a traveling wave. It is noteworthy that in fluid-based thermoacoustic devices, the thermal buffer tube (TBT), whose companion component in solids is the TBS (Fig. 1), acts as a wave scatterer due to the temperature dependence of sound speed of the fluid media [19]. The speed of sound in solids is expressed as $c = \sqrt{E/\rho}$ for longitudinal waves, and has a negligible dependency on temperatures; as such, the TBS is not expected to yield wave scattering effect. However, the length of the TBS l_s does affect the growth ratio of the traveling wave mode in solid-state thermoacoustic devices; in particular, $l_s = 0.45L$ achieves the optimal growth ratio for the setup analyzed herein. A plot of growth ratio β/ω vs. nondimensional TBS length l_s/L can be found in Supplementary Material.

On the other hand, for the resonance rod configuration, only standing-wave thermoacoustic waves can exist since the traveling wave mode is suppressed by the displacement node. In this case, the second mode (also $(\lambda = L)$) is considered, and denoted as *Res – II* (Fig. 2). The presence of a displacement node also decreases the rod's degree of symmetry. Thus, the stage location, while being irrelevant in the looped rod configuration, crucially affects the growth ratio in the standing wave resonance rod. An improper placement of the stage on a resonance rod can lead to a negative growth rate, physically attenuating the oscillations. As Fig. 4 shows, only a proper location falling into the shaded region leads to a positive growth ratio. Other than the stage location, the radius of the rod is also another important factor, which can affect the growth ratio for the resonance rod configuration. In Fig. 3, we show the β/ω vs. R/δ_k relations of a resonance rod for different stage locations as well. The maximum thermoacoustic response is obtained for a stage location $x_s = 0.845L$ (*Res – II*, case A).

Fig. 3 shows that as $R \gg \delta_k$, all the curves, whether the looped or the resonance rod, reach zero due to the weakened thermal contact between the solid medium and the stage. However, as R/δ_k reaches zero (shaded grey region), the stage is very strongly thermally coupled with the elastic wave. As a result, the traveling wave mode dominates. The reason for mode switching will be discussed later in this section. The stability curves also tell that the traveling wave engine has about 4 times higher growth ratio in the limit $R/\delta_k \rightarrow 0$, compared to the standing wave resonance rod (*Res – II*, case A) in which maximal growth ratio is obtained (at $R/\delta_k \approx 2$). The noteworthy improvement on growth ratio is essential to the design of more robust solid state thermoacoustics devices.

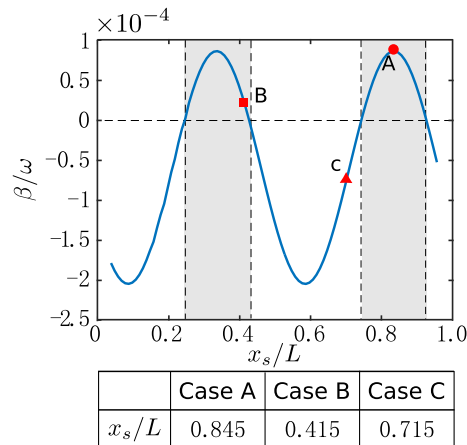


Fig. 4. Plot of the growth ratio versus the normalized stage location for the resonance rod *Res – II* at optimal $R/\delta_k (= 1.8)$. Three specific cases are labeled A, B and C corresponding to the stability curves in Fig. 3. Only the location of the stage falling into the shaded region gives a positive growth ratio.

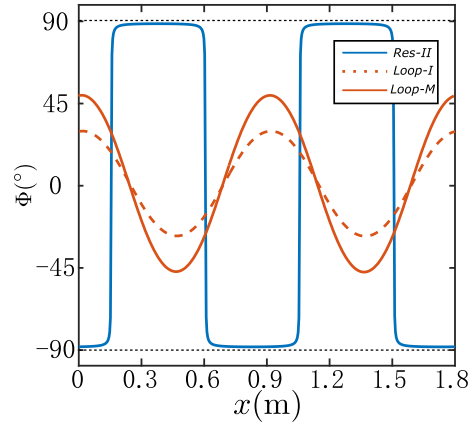


Fig. 5. Plot of the phase difference between negative stress $\bar{\sigma}$ and particle velocity v for an $R = 0.184$ mm resonance rod 'Res - II', an $R = 0.1$ mm looped rod 'Loop - I', and an $R = 0.184$ mm looped rod 'Loop - M'.

Hereafter, the modes or results from Loop - I and Res - II will be taken for values of R of 0.1 mm and 0.184 mm, i.e. R/δ_k of 1.0 and 1.8 respectively.

In classical thermoacoustics, the phase delay between pressure and cross-sectional averaged velocity is an essential controlling parameter of thermoacoustic energy conversion [6,7]. Ceperley [7] stated that the energy conversion process of a traveling wave TA machine resembles that of a Stirling engine with the piston being an air column, while the standing wave engines need a thermal delay to effectively convert energy. In analogy with thermoacoustics in fluids, we use the phase difference Φ between negative stress $\bar{\sigma} = -\sigma = |\hat{\sigma}| \text{Re}[e^{i(\omega t + \phi_{\bar{\sigma}})}]$ and particle velocity $v = |\hat{v}| \text{Re}[e^{i(\omega t + \phi_v)}]$, where $\phi_{\bar{\sigma}}$ and ϕ_v denote the phases of $\bar{\sigma}$ and v respectively, $\Phi = \phi_v - \phi_{\bar{\sigma}}$. Note that a negative stress in solids indicates compression which is equivalent to a positive pressure in fluids. The standing wave component (SWC) and traveling wave component (TWC) of velocity are quantified as $v_s = |\hat{v}| \text{Re}[e^{i(\omega t + \phi_{\bar{\sigma}} + \pi/2)}] \sin \Phi$ and $v_T = |\hat{v}| \text{Re}[e^{i(\omega t + \phi_{\bar{\sigma}})}] \cos \Phi$, which are 90° out-of-phase and in-phase with $\bar{\sigma}$, respectively. In a resonance rod, TWC is negligible because the wave propagation at the extremities is impeded by the clamped boundary condition, the displacement node. However, the non-zero growth rate β will cause a small phase shift, which makes the phase difference Φ close to but not exactly 90° . The blue solid line in Fig. 5 shows the phase difference of a $R = 0.184$ mm resonance rod (Res - II). In the case of a thick looped rod ($R \gg \delta_k$) with a poor degree of thermal contact, the mode shape is much similar to that of a resonance rod because SWC is still dominant and the phase difference is close to 90° . Supplementary Movie 1 shows that the displacement nodes may exist intrinsically in the system without clamped points. However, when the looped rod is sufficiently thin ($R \sim \delta_k$) the traveling wave component plays a dominant role. Thus, the phase delay decreases to 30° at most. The orange dashed line in Fig. 5 shows the phase difference of a $R = 0.1$ mm looped rod (Loop - I). The time history of the displacement along the looped rod in Supplementary Movie 2 shows that, as $R \leq \delta_k$ (small phase difference), the wave mode is dominated by TWC. Fig. 5 also presents an intermediate case (Loop - M, the orange solid line) in which the phase difference of a looped rod whose radius is equal to that of Res - II is shown. The phase difference is 50° at most, indicating that neither TWC nor SWC plays a dominating role so the wave mode is highly mixed.

Supplementary video related to this article can be found at <https://doi.org/10.1016/j.jsv.2019.02.029>.

In the looped rod, the TWC of the thermoacoustically unstable waves increases with respect to the SWC as the degree of thermal contact in the thermoacoustic core, expressed as the ratio of the thermal penetration depth δ_k to the radius R , is increased. This is consistent with Ceperley's classical statement [7]: excellent thermal contact between the stage and the medium is favorable to traveling waves, while standing waves prefer imperfect thermal contact. This can be understood by considering an infinitesimal solid element in the S-seg. shown in Fig. 1, where positive velocity leads to the element moving into a hotter region and, hence, being heated. In a traveling wave, velocity and negative (compressive) stress $\hat{\sigma}$ are in phase, so the solid element undergoes a cycle with compression, heating, expansion and cooling phases distinct from each other, resembling a Stirling cycle. In a standing wave, however, negative stress and velocity have a 90° phase difference, so a thermal delay is necessary to avoid simultaneous compression and heating, and simultaneous expansion and cooling, which would lead to no thermal-to-elastic energy conversion. The thermal delay, or poor thermal contact, is in fact achieved by increasing the radius of the rod. The inward radial heat transfer can be expressed as $\hat{q} = R\rho c_e(i\omega g_k)\hat{T}$. (See Eq. (22) in Supplementary Material). Fig. 6 (a) shows that as the radius decreases, the real part of g_k becomes negligible compared to the large imaginary part, so an element at a temperature lower than the base temperature will instantly absorb heat from the boundary, indicating an excellent thermal contact. Contrarily, as $R/\delta_k \gg 1$, the real and imaginary parts of g_k become comparable (See the inset), leading to a phase/thermal delay, which favors a standing-wave phasing. The change of Φ_m , referring to the maximal phase difference between \hat{v} and $\hat{\sigma}$, with R/δ_k is plotted in Fig. 6 (b); and it is shown that as the thermal contact/rod radius becomes stronger/smaller, the mode in the rod switches from SWC dominated ($\Phi_m \approx 90^\circ$) to TWC dominated ($\Phi_m \approx 30^\circ$). The blue curves for Res - II in Fig. 3 provide another evidence that perfect thermal contact (low R/δ_k) does not promote standing-wave phasing. In the resonance

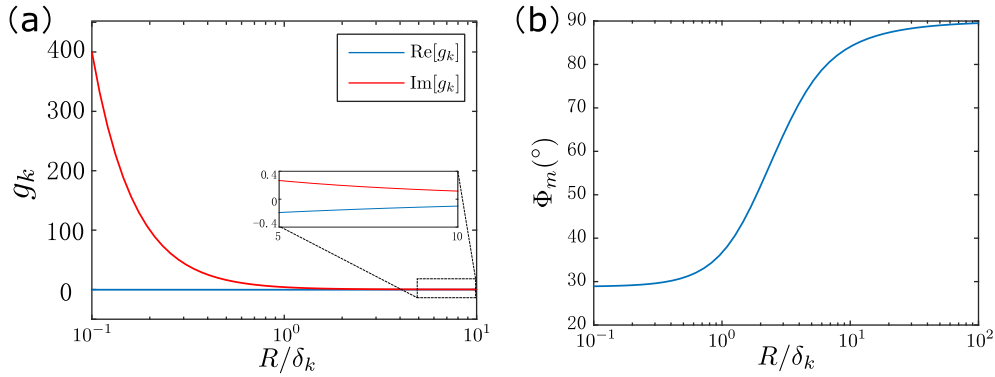


Fig. 6. (a) The real and imaginary parts of the dimensionless complex function g_k vs. the dimensionless radius R/δ_k . g_k is a geometry-dependent function accounting for the radial heat conduction in the S-segment. The high imaginary part of g_k on the left indicates an excellent thermal contact between the medium and the boundary. (b) The maximal value of the phase difference between $\hat{\sigma}$ and \hat{v} vs. the dimensionless radius R/δ_k , showing as the looped rod becomes thinner, the phase difference decreases and eventually TWC dominates.

rod, traveling wave is suppressed by the clamped boundaries; and as $R/\delta_k \ll 1$, β/ω tends to zero, which proves the limited amplification of the standing wave under high degrees of thermal contact.

It is noteworthy that in either the resonance rod or the looped rod, neither a pure standing wave nor traveling wave is ever achieved due to the presence of the base temperature gradient and thermoacoustic production of power. Therefore, when referring to a standing-wave or traveling-wave mode, the latter are intended as the *dominating* contributions to the instability. The *Res – II* mode in the resonance rod is dominated by the SWC with a phase difference close to, but never exactly equal, to 90° and the *Loop – I* mode in the looped rod is dominated by the TWC, with the phase difference at most 30° at a few locations in the domain (Fig. 5).

5. Energy conversions in solid-state thermoacoustic engines

In this section, we explore the energy conversion process in the resonance and the looped rods. The resonance rod, ‘Res’, has a length of 1.8 m, radius of $R = 0.184$ mm and the stage location $x_s = 0.805L$. The looped rod, ‘Loop’, has the same total length, but the radius $R = 0.1$ mm is selected to allow the TWC to dominate. The location of the stage in looped rods does not influence the thermoacoustic response, thus only for illustrative purposes, it is located at $x_s = 0.205L$ so that the TBS does not cross the point where periodicity is applied.

In Section 5.1, we present definitions of heat flux, work flux (mechanical power) and work source for the SSTA system. The latter are then discussed in Section 5.2 within the context of acoustic energy budgets rigorously derived from the governing equations, naturally yielding the consistent expressions of the second order energy norm, energy redistribution term, and the thermoacoustic production and dissipation. The thermal-to-acoustic (or thermodynamic) efficiency, defined as the ratio of the net acoustic energy gain per cycle to the total heat absorbed by the medium, is analyzed for SSTA devices where it is found that the first mode of the traveling wave engine (‘Loop – I’) is more efficient than the second standing wave mode (‘Res – II’).

5.1. Heat flux, mechanical energy and work source

A cycle-averaged heat flux in the axial direction is generated in the S-segment due to its heat exchange with the stage. Neglecting the axial thermal conductivity, the transport of entropy fluctuations due to the fluctuating velocity v_1 (subscript 1 for a first order fluctuating term in time) is the only way heat can be transported along the axial direction [5]. The instantaneous heat flux is expressed in the time domain as

$$q_2 = T_0 \rho_0 (s_1 v_1) [\text{W/m}^2] \quad (8)$$

where the subscript 2 denotes a second-order quantity. Entropy fluctuations in solids are related to temperature and strain rate fluctuations via the following relation from thermoelasticity theory [20]:

$$s_1 = \frac{c_e}{T_0} T_1 + \alpha E \epsilon_1. \quad (9)$$

Substituting Eq. (9) into Eq. (8), q_2 can be expressed in terms of T_1 , v_1 and ϵ_1 . Note that the quantities with subscript 1 are instantaneous and dependent on both radial and axial coordinates, while the hatted quantities \hat{T} , \hat{v} and $\hat{\epsilon}$ are the Fourier amplitudes of the cross-sectional averaged first order fluctuations. The latter can be extracted from the eigenfunctions of the eigenvalue problem (Eqs. (4)–(6)). Under the assumptions: (1) $\beta/\omega \ll 1$, and (2) v_1 is uniform through the cross section, the cycle average of the second order cross-sectionally-averaged products, $\langle a_1 v_1 \rangle_r$, can be evaluated as $\langle \langle a_1 v_1 \rangle_r \rangle = \langle \langle a_1 \rangle_r \langle v_1 \rangle_r \rangle = \frac{1}{2} \text{Re}[\hat{a} \hat{v}^*] e^{2\beta t}$

(e.g. $\langle \langle s_1 v_1 \rangle_r \rangle = \frac{1}{2} \text{Re}[\widehat{s\hat{v}}^*] e^{2\beta t}$), where a is a dummy harmonic variable following the $e^{i\Lambda t}$ convention introduced in Section 3, the superscript $*$ denotes the complex conjugate, and $\langle \rangle$ and $\langle \rangle_r$ are the cycle averaging and cross-sectional averaging, respectively. Note that since hatted quantities already denote cross-sectional averaged quantities in the frequency domain, angular brackets are omitted for quantities such as \widehat{T} , \widehat{v} and $\widehat{\epsilon}$. We want to stress that the uniformity of v_1 through the cross section is necessary for the above evaluation to hold because the cross-sectional average of the product of two first-order terms ($\langle a_1 v_1 \rangle_r$) can be equal to the product of two cross-sectionally averaged terms ($\langle a_1 \rangle_r \langle v_1 \rangle_r$) only if one of the two terms is uniform in the cross section. Contrary to the fluids case, where viscous effects cause a non-uniform distribution of velocity along radial direction, in the case of longitudinal waves in solids, it is correct to assume a uniform radial velocity distribution.

We obtain $\langle q_2 \rangle = \widetilde{Q} e^{2\beta t}$, where

$$\widetilde{Q} = \frac{1}{2} \rho_0 c_e \text{Re}[\widehat{T\hat{v}}^*] + \frac{1}{2} T_0 \alpha E \text{Re}[\widehat{\epsilon\hat{v}}^*] \quad [\text{W/m}^2]. \quad (10)$$

The total heat flux through the cross section of the rod is

$$\dot{Q} = \int_A \langle q_2 \rangle dS = A \langle q_2 \rangle \quad [\text{W}]. \quad (11)$$

The second equality holds because the eigenfunctions are all cross-section-averaged quantities. We note that \dot{Q} is a function of the axial position x .

The instantaneous mechanical power carried by the wave is defined as

$$I_2 = (-\sigma_1) v_1 = \overline{\sigma}_1 v_1. \quad [\text{W/m}^2] \quad (12)$$

This quantity physically represents the rate per unit area at which work is done by an element onto its neighbor. It can be also called ‘work flux’ because it shows the work flow in the medium as well. When an element is compressed ($\overline{\sigma} > 0$), it ‘pushes’ its neighbor so that a positive work is done on the adjacent element. A notable fact is that there is a directionality to I_2 , which depends on the direction of v_1 .

Similarly, the cycle-average mechanical power $\langle I_2 \rangle$ can be expressed as $\langle I_2 \rangle = \widetilde{I} e^{2\beta t}$, where

$$\widetilde{I} = \frac{1}{2} \text{Re}[\widehat{\sigma\hat{v}}^*] \quad [\text{W/m}^2]. \quad (13)$$

The total mechanical power through the cross section I of the rod is given by

$$I = \int_A \langle I_2 \rangle dS = A \langle I_2 \rangle \quad [\text{W}]. \quad (14)$$

The work source can be further defined as the gradient of the mechanical power as

$$w_2 = \frac{\partial I_2}{\partial x} \quad [\text{W/m}^3]. \quad (15)$$

By expanding Eq. (15), w_2 can be further expressed as

$$w_2 = \frac{\partial \overline{\sigma}_1}{\partial x} v_1 + \frac{\partial v_1}{\partial x} \overline{\sigma}_1 \quad (16)$$

The first term of w_2 vanishes after applying cycle-averaging, because according to the momentum conservation (Eq. (5)), $\partial \sigma_1 / \partial x$ and v_1 are 90° out of phase under the assumption that the small phase difference caused by the non-zero β can be neglected due to: $\beta/\omega \ll 1$. The remaining term is equivalent to $\overline{\sigma}_1 \frac{\partial \epsilon_1}{\partial t}$, i.e.

$$\frac{\partial v_1}{\partial x} \overline{\sigma}_1 = \overline{\sigma}_1 \frac{\partial \epsilon_1}{\partial t}, \quad (17)$$

whose cycle average is consistent with the cycle-averaged volume change work defined in Ref. [4].

The cross sectional integral of the work source is given by

$$W = \int_A \langle w_2 \rangle dS = A \langle w_2 \rangle \quad [\text{W/m}]. \quad (18)$$

Fig. 7 shows the cycle-averaged quantities: heat flux \widetilde{Q} and mechanical power \widetilde{I} of a traveling wave engine (‘Loop’) and a standing wave one (‘Res’). Note that the quantities indicated with $\widetilde{}$ satisfy the assumption of cycle averaging: $\langle \rangle = \widetilde{} e^{2\beta t}$. Fig. 7(a) and (c) illustrate that heat flux only exists in the S-segment and that wave-induced transport of heat occurs from the hot to the cold heat exchanger. The negative values in the S-segment in (a) and (c) are due to the fact that the hot exchanger is on the right side of the cold one, so heat flows to the negative x direction in that case. The non-zero spatial gradient in \widetilde{Q} in the S-segment proves that there is heat exchange happening on the boundary of this segment because the heat flux in the axial direction is not balanced on its own.

Fig. 7(d) shows the mechanical power in the standing wave engine. The positive slope of \widetilde{I} in the S-segment elucidates the fact that the work generated in this region is positive, as discussed in detail in Section 5.2. This amount of work drops along the

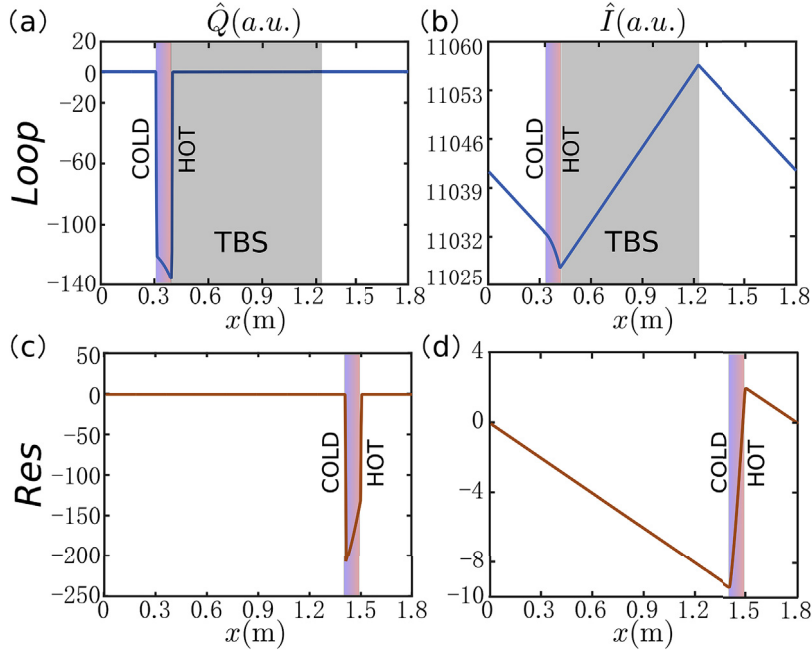


Fig. 7. Cycle-averaged heat flux \tilde{Q} and mechanical power \tilde{I} in the frequency domain (arbitrary units) for the looped rod ‘Loop’ and the resonance rod ‘Res’, respectively. These components are evaluated from eigenfunctions from the stability analysis (Eqs. (4)–(6)). The color gradient strips indicate the location of S-segment, and the shaded grey strips indicate the location of the TBS in ‘Loop’.

axial direction in the remaining segments at the spatial rate of $d\tilde{I}/dx$. The work drop in the hot and cold segments balances the accumulation of energy because there is no radial energy exchange in these sections. Clearly, if there is no energy growth, the slope of \tilde{I} should be zero in these sections, as also discussed in Section 5.2.

The work flow in the traveling wave engine, as Fig. 7(b) shows, has a very large value, which is due to the fact that negative stress $\bar{\sigma}$ and particle velocity v have a phase difference much smaller than 90° (Fig. 5). This means that a nearly uniform work flow is circulating the ‘Loop’ carried by the wave dominated by TWC. Contrarily to the standing wave case, the slope of \tilde{I} is negative in the S-segment, because it is balancing the positive work created by I against the temperature gradient in the TBS. The volumetric integration of the work source w , i.e. the spatial integration of W along the rod, should be zero because, globally, there is no energy output in the system. All the energy converted from the heat in the S-segment should eventually lead to a uniformly distributed perturbation energy growth. More discussions will be addressed in the following section.

5.2. Acoustic energy budgets

To derive the acoustic energy budgets, we first recast Eqs. (5) and (6) in the time domain following the procedure by Ref. [21] as

$$\frac{\partial v_1}{\partial t} = -\frac{1}{\rho} \frac{\partial \bar{\sigma}_1}{\partial x}, \quad (19)$$

$$\frac{\partial \bar{\sigma}_1}{\partial t} = -E(1 + \alpha \gamma_G T_0) \frac{\partial v_1}{\partial x} - \alpha E \frac{dT_0}{dx} v_1 + \frac{\alpha E}{R \rho c_\epsilon} q_1, \quad (20)$$

where, $q_1 = 2\kappa \frac{\partial T_1}{\partial r}|_{r=R}$ indicates the conductive heat flux at the medium-stage interface.

Multiplying Eq. (19) by ρv_1 and Eq. (20) by $\bar{\sigma}_1 E^{-1} (1 + \alpha \gamma_G T_0)^{-1}$, and adding them gives

$$\frac{\partial \mathcal{E}_2}{\partial t} + \frac{\partial I_2}{\partial x} + \mathcal{R}_2 = \mathcal{P}_2 - \mathcal{D}_2, \quad (21)$$

where

$$\mathcal{E}_2 = \frac{1}{2} \rho v_1^2 + \frac{1}{2} \frac{1}{E(1 + \alpha \gamma_G T_0)} \bar{\sigma}_1^2, \quad (22)$$

$$I_2 = \bar{\sigma}_1 v_1, \quad (23)$$

$$\mathcal{R}_2 = \frac{\alpha}{1 + \alpha\gamma_G T_0} \frac{dT_0}{dx} I_2, \quad (24)$$

$$\mathcal{P}_2 - \mathcal{D}_2 = \frac{\alpha}{1 + \alpha\gamma_G T_0} \frac{1}{R\rho c_\epsilon} q_1 \bar{\sigma}_1. \quad (25)$$

$\mathcal{E}_2, I_2, \mathcal{R}_2, \mathcal{P}_2$ and \mathcal{D}_2 are the second order energy norm, work flux, energy redistribution term, thermoacoustic production and dissipation, respectively. Note that the work flux shown in Eq. (23) is consistent with the heuristic definition adopted in the previous section (Eq. (12)). With the harmonic convention $\langle \rangle_1 = e^{(\beta+i\omega)t} \langle \rangle$ and the assumption $\beta/\omega \ll 1$, taking the cycle averaging of Eq. (21) yields

$$2\beta\tilde{\mathcal{E}} + \frac{d\tilde{I}}{dx} + \tilde{\mathcal{R}} = \tilde{\mathcal{P}} - \tilde{\mathcal{D}}, \quad (26)$$

where $\tilde{\mathcal{E}}, \tilde{\mathcal{R}}, \tilde{I}, \tilde{\mathcal{P}}$, and $\tilde{\mathcal{D}}$ are transformed from the cycle averages of the cross-sectionally-averaged second order terms in Eqs. (22)–(25), following the assumption of cycle averaging: $\langle \langle \rangle_2 \rangle = \tilde{\langle \rangle} e^{2\beta t}$. They are expressed as

$$\tilde{\mathcal{E}} = \frac{1}{2} \rho |\hat{v}|^2 + \frac{1}{2} \frac{1}{E(1 + \alpha\gamma_G T_0)} |\hat{\sigma}|^2 [\text{W/m}^3], \quad (27)$$

$$\tilde{I} = \frac{1}{2} \text{Re}[\hat{\sigma} \hat{v}^*] [\text{W/m}^2], \quad (28)$$

$$\tilde{\mathcal{R}} = \frac{1}{2} \frac{\alpha}{1 + \alpha\gamma_G T_0} \frac{dT_0}{dx} \text{Re}[\hat{\sigma} \hat{v}^*] [\text{W/m}^3], \quad (29)$$

$$\tilde{\mathcal{P}} = \frac{1}{2} \frac{1}{1 + \alpha\gamma_G T_0} \{ \text{Re}[g_k] \text{Re}[\hat{\sigma}(\hat{v} \hat{\epsilon})^*] + \text{Im}[g_k] \text{Im}[\hat{\sigma}(\hat{v} \hat{\epsilon})^*] \} [\text{W/m}^3], \quad (30)$$

$$\tilde{\mathcal{D}} = \frac{\omega}{2} \frac{1}{E(1 + \alpha\gamma_G T_0)} |\hat{\sigma}|^2 \text{Im}[g_k] [\text{W/m}^3]. \quad (31)$$

The details of the derivations of Eqs. (26)–(31) can be found in the supplementary material.

The growth rate can be recovered via

$$\beta_{\text{EB}} = \frac{\tilde{\mathcal{P}} - \tilde{\mathcal{D}} - (\frac{d\tilde{I}}{dx} + \tilde{\mathcal{R}})}{2\tilde{\mathcal{E}}}. \quad (32)$$

As Fig. 8 shows, the growth rates β_{EB} calculated from Eq. (32) are within 0.4% from the direct output of the eigenvalue problem (Eqs. (4)–(6)) in both the standing wave and the traveling wave configurations, which validates the consistency of the derivations in this section.

From the physical point of view, the significance of the terms in Eq. (26) are illustrated as following. $2\beta\tilde{\mathcal{E}}$ quantifies the rate of energy accumulation, $d\tilde{I}/dx$ is the work source defined in the previous section, $\tilde{\mathcal{R}}$ is an energy redistribution term. $\tilde{\mathcal{P}}$ and $\tilde{\mathcal{D}}$ are the thermoacoustic production and dissipation, respectively. The energy redistribution term in the acoustic energy budgets of solid thermoacoustics cannot be found in the fluid counterpart of the same equations [21]. This term is absent in fluids because it is canceled in the algebraic derivations by expressing the variation of mean density according to the ideal gas law, as a function of the mean temperature gradient. On the other hand, in solid-state thermoacoustics, the heat-induced

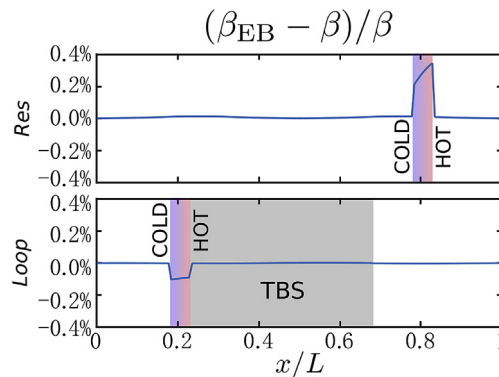


Fig. 8. The relative difference of the growth rates estimated from the energy budgets β_{EB} and directly retrieved from the eigenvalue problem in Eqs. (4)–(6) for the standing wave configuration ('Res') and the traveling wave configuration ('Loop').

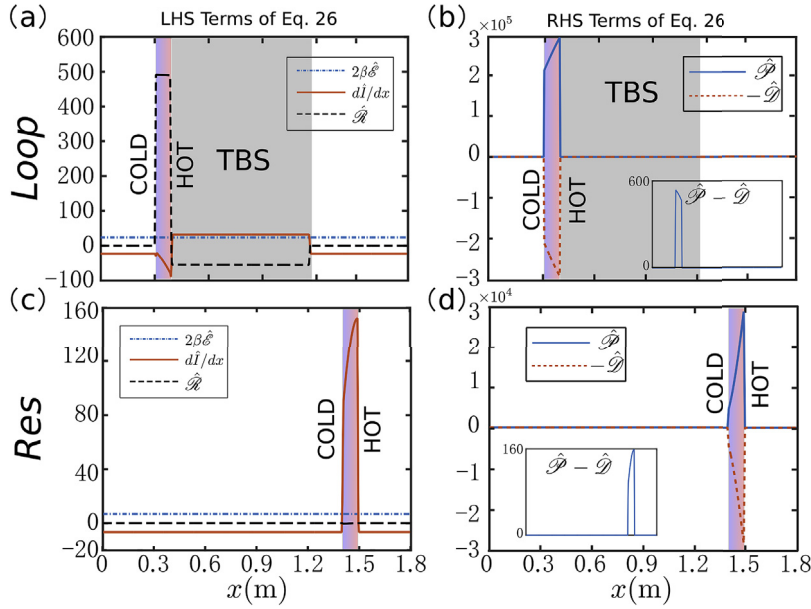


Fig. 9. The terms in the acoustic energy budgets (Eq. (26)) for (a) and (b) the traveling wave configuration ('Loop') and, (c) and (d) the standing wave configuration ('Res'). The insets in (b) and (d) plot the difference of the thermoacoustic production $\hat{\mathcal{P}}$ and dissipation $\hat{\mathcal{D}}$ in both configurations. The spatial integration of $\hat{\mathcal{P}} - \hat{\mathcal{D}}$ yields the total energy accumulation rate (see Eq. (33)).

density variation is neglected and the impact of the temperature gradient is manifest in the stress-strain constitutive relation. It is proved numerically that the spatial integration of this term is zero (see Supplementary Material), so it does not produce or dissipate energy, but just *redistributes* it. In summary, it represents the work created by the acoustic flux acting against the temperature gradient. Fig. 9 plots every term in the acoustic energy budgets (Eq. (26)) in the standing wave and traveling wave configurations, respectively.

The values of $\hat{\mathcal{P}}$ and $\hat{\mathcal{D}}$ are non-zero only in the S-segment. The dissipation $\hat{\mathcal{D}}$ is due to wall heat transfer, which is a conductive loss. Although they are very similar in the S-segment, there exists a small difference between them. Thus, from a thermal standpoint, as a given amount of heat is transported through this section, a small portion of it (proportional to $\hat{\mathcal{P}} - \hat{\mathcal{D}}$) is converted into wave energy which accumulates in the rod, hence sustaining growth. Regarding $\hat{\mathcal{R}}$, a remarkable difference with thermoacoustic waves in fluids is present. In the latter case [21], $\hat{\mathcal{R}}$ can be explicitly expressed as the weighted combination of a standing wave ($\text{Im}[\hat{p}^* \hat{U}]$) and traveling wave ($\text{Re}[\hat{p}^* \hat{U}]$) (Eq. (4.13a) in Ref. [21]), where p and U are the pressure and flow rates, respectively, so the traveling-/standing-wave contribution of the thermoacoustic production $\hat{\mathcal{P}}$ is zero when the mode is purely standing/traveling. However in solids, the two terms on the right hand side of Eq. (30) do not depend on the wave phasing, since whether they are zero or not only depends on if there is thermal coupling (if \hat{T} is zero). So these two terms can not be considered as the TWC and SWC contributions of the thermoacoustic energy production $\hat{\mathcal{P}}$.

As can be seen, $2\beta\hat{\mathcal{E}}$ is flat, meaning that the rate of the energy accumulation along the rod is uniform and exponential in time, consistent with the eigenvalue *ansatz*.

In the standing wave configuration, the work flux gradient $d\hat{l}/dx$ peaks in the S-segment, and has a constant negative value out of the S-segment. As foreshadowed by the discussions in the previous section, this distribution means that $d\hat{l}/dx$ adjusts itself so that β is uniform. In other words, energy is accumulated everywhere at the same rate.

Neglecting the small phase shift caused by β , the energy redistribution $\hat{\mathcal{R}}$ does not exist in the standing wave configuration because of the 90° phase difference between $\hat{\sigma}$ and \hat{v} . Locally, the produced work in the S-segment, is converted from the most of the net production $\hat{\mathcal{P}} - \hat{\mathcal{D}}$. The remaining of $\hat{\mathcal{P}} - \hat{\mathcal{D}}$ transforms to the accumulated energy in this small segment. Outside the S-segment, the negative value of $d\hat{l}/dx$ is exactly the same as the rate of the energy accumulation to keep the condition of zero local net production.

In the traveling wave configuration, the energy conversion becomes different because of the existence of the TBS. The TBS creates a temperature drop, which makes the energy redistribution term non zero in this section. To balance the negative value in the TBS, it peaks up in the S-segment so that the spatial integration is zero. In the TBS, the shape of the work flux gradient is the mirror image of that of the energy redistribution term because the addition of these two terms should be the negative of the spatially uniform energy accumulation rate. For the work flux gradient itself, a negative distribution in the S-segment is necessary to balance the positive redistributed work in the TBS so that the spatial integration is zero. The above supplements the explanations in the previous section on why the work source is negative in the S-segment.

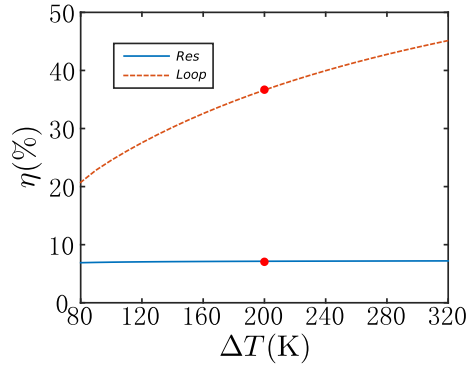


Fig. 10. The efficiencies of the traveling wave configuration ('Loop') and the standing wave configuration ('Res') at different temperature difference ΔT . The efficiencies are 37% and 7%, respectively at $\Delta T = 200\text{K}$ (The red dots).

Globally, in both configurations, given that both the spatial integrations of the work flux gradient and the energy redistribution terms are zero, the total net production $\int_0^L (\tilde{\mathcal{P}} - \tilde{\mathcal{D}})dx$ only leads to the accumulation of energy

$$\int_0^L 2\beta \tilde{\mathcal{E}} dx = \int_0^L (\tilde{\mathcal{P}} - \tilde{\mathcal{D}}) dx. \quad (33)$$

5.3. Efficiency

Generally, efficiency is defined as the ratio of work done to thermal energy consumed. However, since there is no energy harvesting element in the system, the rod has no work output. Thus, we take the accumulated energy, which could be potentially converted to energy output, as the numerator of the ratio. For the denominator, limited to the 1D assumption, the thermal energy consumed is not available directly from the quasi-1D model because the evaluation of the radial heat conduction at the boundary is lacking. Swift [5] suggested that the heat flux \dot{Q} could be considered as uniform for a short stack, which is approximately equal to the consumed thermal energy. Thus, we use the averaged \dot{Q} over the S-segment, an estimate of the consumed thermal energy, as the denominator of the efficiency. As a result, the efficiency η is expressed as

$$\eta = \frac{A \int_0^L \frac{\partial \mathcal{E}_2}{\partial t} dx}{\frac{1}{l_s} \int_{x_s - \frac{l_s}{2}}^{x_s + \frac{l_s}{2}} \dot{Q} dx} \quad (34)$$

$$= \frac{\int_0^L 2\beta \tilde{\mathcal{E}} dx}{\frac{1}{l_s} \int_{x_s - \frac{l_s}{2}}^{x_s + \frac{l_s}{2}} \tilde{Q} dx}. \quad (35)$$

Although this definition is the best estimate we could make based on the quasi-1D model, we highlight that fully nonlinear 3D simulations are capable of providing more accurate estimates of the efficiency.

Fig. 10 shows the efficiencies of 'Loop' and 'Res' at different temperature difference $\Delta T = T_h - T_c$. It can be seen from this plot that (1) the efficiency of the traveling wave configuration 'Loop' is much higher than that of the standing wave configuration Res, which is consistent with the conclusions drawn in fluids, and (2) for the traveling wave configuration, the efficiency goes up with ΔT increasing, while for the standing wave one, the efficiency is insensitive to the change of ΔT . For the cases studied in the previous sections ($\Delta T = 493.15\text{ K} - 293.15\text{ K} = 200\text{ K}$), the efficiencies η are 5% and 7% for 'Loop' and 'Res', respectively, as the red dots show in Fig. 10.

Considering that the material properties of solids are much more tailorable than fluids, the authors expect that the efficiency of SSTA can be improved by designing an inhomogeneous medium having optimized mechanical and thermal thermoacoustic properties.

6. Conclusions

In this study, we have shown numerical evidence of the existence of traveling wave thermoacoustic oscillations in a looped solid rod. The growth ratio of a full wavelength traveling wave in a looped rod is found to be significantly larger than that of a full wavelength standing wave in a resonance rod. The phase delay in the looped rod between negative stress and particle velocity, which controls the value of TWC, is at most 30° under the situation that the stage is $5\%L$ long and $\Delta T_0 = 200\text{K}$. Heat flux, mechanical power and work source are derived in analogous ways to their counterparts in fluids. The perturbation acoustic

energy budgets are performed to interpret the energy conversion process of SSTA engines. The efficiency of SSTA engines is defined based on the rigorously derived energy budgets. The traveling wave SSTA engine is found to be more efficient than its standing wave counterpart. To conclude, this study confirms the theoretical existence of traveling wave thermoacoustics in a solid looped rod which could open the way to the next generation of highly-robust and ultra-compact traveling wave thermoacoustic engines and refrigerators.

Acknowledgments

H. Hao would like to thank Prateek Gupta for the fruitful discussions and his helpful comments on acoustic energy budgets.

Appendix A. Supplementary data

Supplementary data related to this article can be found at <https://doi.org/10.1016/j.jsv.2019.02.029>.

References

- [1] J.L. Rayleigh, The explanation of certain acoustical phenomena, *Nature* 18 (1878) 319–321.
- [2] T. Poinot, D. Veynante, in: *Theoretical and Numerical Combustion*, R. T. Edwards, Inc., Philadelphia, PA, 2011.
- [3] P. Rijke, LXXI. Notice of a new method of causing a vibration of the air contained in a tube open at both ends, *Philos. Mag. Ser. 17* (116) (1859) 419–422.
- [4] H. Hao, C. Scalo, M. Sen, F. Semperlotti, Thermoacoustics of solids: a pathway to solid state engines and refrigerators, *J. Appl. Phys.* 123 (2) (2018) 024903. URL <https://doi.org/10.1063/1.5006489>.
- [5] G. Swift, Thermoacoustic engines, *J. Acoust. Soc. Am.* 84 (4) (1998) 1145–1180 URL, <https://doi.org/10.1121/1.396617>.
- [6] T. Yazaki, A. Iwata, T. Maekawa, A. Tominaga, Traveling wave thermoacoustic engine in a looped tube, *Phys. Rev. Lett.* 81 (15) (1998) 3128–3131 URL, <https://doi.org/10.1103/PhysRevLett.81.3128>.
- [7] P. Ceperley, A pistonless stirling engine—the traveling wave heat engine, *J. Acoust. Soc. Am.* 66 (5) (1979) 1508–1513 URL, <https://doi.org/10.1121/1.383505>.
- [8] S. Backhaus, G. Swift, A thermoacoustic-stirling heat engine: detailed study, *J. Acoust. Soc. Am.* 107 (6) (2000) 3148–3166 URL, <https://doi.org/10.1121/1.429343>.
- [9] D. Gedeon, *DC Gas Flows in Stirling and Pulse Tube Cryocoolers*, Springer US, Boston, MA, 1997. URL https://doi.org/10.1007/978-1-4615-5869-9_45.
- [10] Y.L. Ju, C. Wang, Y. Zhou, Dynamic Experimental Study of the Multi-Bypass Pulse Tube Refrigerator with Two-Bypass Tubes, Springer US, Boston, MA, 1998. URL https://doi.org/10.1007/978-1-4757-9047-4_256.
- [11] A. Ravex, J.M. Poncet, I. Charles, P. Bleu  , Development of Low Frequency Pulse Tube Refrigerators, Springer US, Boston, MA, 1998. URL https://doi.org/10.1007/978-1-4757-9047-4_247.
- [12] J. Olson, G. Swift, Acoustic streaming in pulse tube refrigerators: tapered pulse tubes, *Cryogenics* 37 (12) (1997) 769–776 URL, [https://doi.org/10.1016/S0011-2275\(97\)00037-4](https://doi.org/10.1016/S0011-2275(97)00037-4).
- [13] S. Boluriaan, P. Morris, Acoustic streaming: from Rayleigh to today, *Int. J. Aeroacoust.* 2 (3–4) (2003) 255–292 URL, <https://doi.org/10.1260/14754720322986142>.
- [14] C. Scalo, S. Lele, L. Hesselink, Linear and nonlinear modelling of a theoretical travelling-wave thermoacoustic heat engine, *J. Fluid Mech.* 766 (2015) 368–404 URL, <https://doi.org/10.1017/jfm.2014.745>.
- [15] G. Swift, Analysis and performance of a large thermoacoustic engine, *J. Acoust. Soc. Am.* 92 (3) (1992) 1551–1563 URL, <https://doi.org/10.1121/1.403896>.
- [16] N. Rott, Damped and thermally driven acoustic oscillations in wide and narrow tubes, *Z. Angew. Math. Phys.* 20 (2) (1969) 230–243 URL, <https://doi.org/10.1007/BF01595562>.
- [17] B. Yates, *Thermal Expansion*, Plenum Press, New York, NY, 1972.
- [18] J. Lin, C. Scalo, L. Hesselink, High-fidelity Simulation of an Ultrasonic Standing-Wave Thermoacoustic Engine with Bulk Viscosity Effects, Grapevine, TX, 2017. URL <https://doi.org/10.2514/6.2017-0929>.
- [19] G. Penelet, S. Job, V. Gusev, P. Lotton, M. Bruneau, Dependence of sound amplification on temperature distribution in annular thermoacoustic engines, *Acust. Acta Acust* 91 (3) (2005) 567–577.
- [20] M. Biot, Thermoelasticity and irreversible thermodynamics, *J. Appl. Phys.* 27 (3) (1956) 240–253 URL, <https://doi.org/10.1063/1.1722351>.
- [21] P. Gupta, G. Lodato, C. Scalo, Spectral energy cascade in thermoacoustic shock waves, *J. Fluid Mech.* 831 (2017) 358–393 URL, <https://doi.org/10.1017/jfm.2017.635>.